Materials Characterization 144 (2018) 448–460

Contents lists available at ScienceDirect

Materials Characterization

journal homepage: www.elsevier.com/locate/matchar

Three-dimensional grain mapping of open-cell metallic foam by integrating synthetic data with experimental data from high-energy X-ray diffraction microscopy

Jayden C. Plumb[a], Jonathan F. Lind[b], Joseph C. Tucker[c], Ron Kelley[d], Ashley D. Spear[a,*]

[a] Department of Mechanical Engineering, University of Utah, Salt Lake City, UT 84112, USA
[b] Lawrence Livermore National Laboratory, 7000 East Avenue, L-342, Livermore, CA 94550, USA
[c] Exponent, Inc., 149 Commonwealth Dr., Menlo Park, CA 94025, USA
[d] Thermo Fisher Scientific, 5250 NE Dawson Creek Drive, Hillsboro, OR 97124, USA

ARTICLE INFO

Keywords:
3D characterization
3D image analysis
Aluminum foam
HEDM
X-ray synchrotron radiation

ABSTRACT

The complex mechanical response of open-cell foams depends strongly on the hierarchy of length scales inherent in them, from engineering-part scale to the ligament scale through the grain scale down to the crystal-lattice scale. A first step toward understanding and predicting the coordinated mechanical response across length scales requires characterizing the open-cell foam structure in three dimensions at relevant scales. Here, we present an initial attempt to digitally represent a physically-realized aluminum alloy foam in terms of both its geometry/topology as well as its underlying crystallographic orientations by integrating several advanced techniques. Specifically, we use a combination of X-ray computed tomography and X-ray diffraction microscopy in conjunction with synthetic grain mapping. Experimental investigation of the foam shows relatively large grain sizes with respect to the ligament length scale, implying that competing mechanics at different length scales (i.e. grain scale vs. ligament scale) will need to be fully incorporated to understand the mechanical behavior of the foam. The integration of non-destructive measurement techniques with synthetic-data generation provides a path toward realistic modeling of bulk samples of open-cell metal foam resolved at the scale of individual grains.

1. Introduction

Open-cell metallic foams are low-density, structural-material systems that derive their mechanical properties from a combination of their parent alloy and their structural topology and morphology [1]. The topology of open-cell metallic foams can range from ordered (as in lattices) to stochastic. A network of interconnected ligaments, or struts, gives rise to a hierarchical structure of the foams — viz., the component scale of the engineered part, the topological and morphological scales of the foam, and the grain scale of individual ligaments. Because of their low-density hierarchical structure, open-cell metallic foams have been used in a wide range of multifunctional applications [2-4]. For example, in addition to serving as light-weight, load-bearing structures, they can serve concurrently as electrodes for energy-storage devices [5], as hosts for newly generated bone and blood vessels in biomedical implants [6-8], or as impact absorbers and noise insulators for advanced high-speed ground transportation [4], to name a few.

The characterization of grain structure for fully dense metallic alloys is considered by many to be routine practice. Characterization using electron microscopy, for example, has become an instrumental part of research programs that require grain-scale measurements to understand crystallographic texture, the evolution of deformation mechanisms like slip and twinning, and microstructure-sensitive crack formation under both monotonic and cyclic loading. The topological complexities of open-cell metallic foams render these hierarchically structured materials more difficult to characterize at the crystalline level compared to fully dense samples. As an example, very little information exists on the crystallographic texture of open-cell metallic foams, which the authors postulate could be due in part to the difficulty in acquiring statistically significant data using traditional electron-backscatter diffraction (EBSD) techniques. This is mainly because: 1) compared to closed-cell foam or fully dense metal, open-cell foam is challenging to prepare for EBSD-data acquisition due to the sparse and fragile network of ligaments, and 2) a successfully polished section of open-cell foam does not yield statistically significant data for texture analysis since the amount of material per nominal cross section is quite

* Corresponding author.
E-mail address: ashley.spear@utah.edu (A.D. Spear).

https://doi.org/10.1016/j.matchar.2018.07.031
Received 8 May 2018; Received in revised form 22 July 2018; Accepted 23 July 2018
Available online 27 July 2018
1044-5803/

small (< 5% in high-porosity foams). This, perhaps, explains why there are relatively little grain-scale data for open-cell metallic foams compared to their fully dense counterparts. Furthermore, the destructive nature of conventional EBSD precludes the ability to test intact samples of foam or individual ligaments, which will be important for linking structure to mechanical properties.

While the vast majority of characterization studies of open-cell metallic foams have focused solely on the structural topology/morphology of the foams, treating each ligament as a material continuum (e.g. Refs. [9-14]), there have been some studies involving grain-scale observations of such foams. For example, Zhou et al. [15,16] used scanning electron microscopy (SEM) and etching techniques to observe grain-boundary morphology on polished planes of individual ligaments and vertices of foam samples. They found the grains to be relatively large, with nearly one grain spanning entire ligaments in some instances, which is consistent with earlier observations by Nieh et al. [17]. Work by Amsterdam et al. [18] also corroborated Zhou's findings regarding grain size in metallic foams, and the researchers postulated that propensity for intergranular fracture depends upon the non-uniform stress distribution within a ligament under shear loading as well as the distribution of grain-boundary precipitates. Shortly thereafter, Krishna et al. [19] investigated the effect of heat treatment on the microstructure and mechanical properties of metallic foams under free and constrained compression. SEM was used to image the grain structure within individual ligaments of the foams. They found that Vicker's hardness of individual ligaments varied among foams of different pore density due to microstructural inhomogeneity among the foams. Also, the researchers found that heat treating the foams at high temperatures for a long period of time (essentially overaging the foams) led to cracking along grain boundaries, where brittle oxide layers had formed. More recently, Fischer et al. [20] studied the effect of casting and mold temperature on the formation of eutectic silicon particles and corresponding mechanical properties for investment-cast open-cell aluminum foams. The researchers found that increasing the casting temperature and decreasing the mold temperature increased both the effective plateau stress and the specific energy absorption of the foams, which they relate to a combination of increased ligament diameter and reduced number of eutectic silicon particles. While these studies provide critical grain-scale insight into deformation and cracking mechanisms in open-cell metallic foams, crystal-orientation data were not considered.

Despite the challenges mentioned above, some researchers have successfully analyzed crystal structure within individual ligaments of open-cell metallic foams through careful sample preparation and EBSD analysis. In 2004, Goussery et al. [21] investigated the grain-size effect on mechanical properties of open-cell nickel foams having hollow struts with strut-wall thicknesses ranging from 8 to 11 μm. In addition to using backscattered electron imaging to observe grain boundaries, the researchers used EBSD to quantify the crystallographic texture within a specific cross section of individual struts. Results from the measurements showed no preferred crystallographic orientation (i.e. texture) in the nickel foams, which had been produced by nickel magnetron sputtering on a polyurethane foam. The researchers also characterized the yield strength of the foams as a function of grain size, where different grain sizes were achieved through various heat treatments. They found that the yield strength of the foams followed a typical Hall-Petch relationship as long as the grain size was smaller than the strut-wall thickness. In 2014, Jung et al. [22] collected crystallographic data on an open-cell aluminum foam that had been electrochemically coated with nickel. In that work, EBSD data were collected on planes within an individual ligament of the foam. This was done to quantify grain growth and crystallographic texture of the nickel coating in an effort to explain previously observed improvements in mechanical behavior of nickel-coated foams compared to non-coated aluminum foams. Very recently, Matheson et al. [23] used EBSD analysis to compare the grain structure in stochastic open-cell aluminum foams produced via investment casting versus topologically identical foams produced using laser powder bed fusion, or additive manufacturing. Results from that study revealed a much higher density of grain boundaries per ligament in the additively manufactured foam than the investment-cast foam, which is one explanation for the dramatic difference in macroscopic compressive behavior between the two types of foam.

The above-described studies reveal two important conclusions that serve to motivate the work presented here. First, for investment-cast foams, the grain sizes can be quite large relative to the ligament size. This suggests that the mechanical response and fracture behavior could be influenced by the grain structure due to size effects. Second, there remains a need for grain-scale data to help elucidate the role of grain structure and crystallography on physical behavior of open-cell metallic foams across multiple length scales. Grain-scale data in three dimensions is of particular interest given the three-dimensional (3D) nature of the foam geometries and deformation in these hierarchical structural-materials [24].

The objective of this work is to present a methodology and novel results pertaining to the 3D grain structure of an open-cell, investment-cast, aluminum foam. The experimental portion of the methodology leverages a synchrotron-based technique called far-field high-energy X-ray diffraction microscopy (HEDM) [25-31] to make unprecedented measurements of the 3D crystal structure of an open-cell metallic foam. The information from the HEDM measurements is used to populate additional foam volume with synthetic-grain structure. The fusion of data derived from experiment and synthetic-grain mapping enables digital representation of the hierarchical structure of a relatively bulk sample of foam. Full characterization in three dimensions at multiple length scales has the potential to elucidate the mechanical behavior of such foam by considering each length-scale deformation mechanism at play. Such understanding will be key to establishing process-structure-property relationships for investment-cast foams.

2. Materials and Methods

The overall objective of the experimental methodology is to map the 3D grain structure within individual ligaments of an open-cell aluminum foam using data from HEDM, augmented with synthetic data produced based on knowledge of the measured grain population. The material of interest is an open-cell foam of aluminum alloy 6101. The foam is produced using investment casting, whereby a sacrificial polymer template is used to create a ceramic mold of the foam. The aluminum is then cast using the mold. Upon solidification, the ceramic mold is removed and the aluminum foam remains. The foam is then subjected to a T6 heat treatment. The foam sample used in this study is reported to have a nominal linear pore density of 40 pores per inch (ppi), or 1.6 pores per millimeter, and a bulk, nominal density in the range of 6–8 %.

HEDM measurements for this experiment were carried out at Sector 1-ID of the Advanced Photon Source (APS) at Argonne National Laboratory, where the width of the X-ray beam is less than 2 mm. Generally, samples measured using HEDM are designed such that the volume of interest (often, an entire a gage section) will remain within the beam width throughout a full rotation to characterize completely all grains within that volume. This constraint poses a significant challenge for measuring an intact volume of ultra-low-density cellular metal, in which a complete 3D pore is nearly the same size as the X-ray beam and, in some cases, can exceed the beam width. To that end, the following high-level steps have been implemented in this work to map the grain structure for a relatively bulk volume of foam:

1. Image a relatively large volume of foam using a lab-source X-ray computed tomography (CT) system to create a baseline reconstruction of the foam geometry in a global reference frame.
2. Physically extract individual ligaments from a subregion of the foam using a mesoscale milling procedure.

3. Map grain centers and crystal orientations in each of the extracted ligaments using synchrotron-source HEDM.
4. Transform the grain centers and crystal orientations from the local ligament frame to the global reference frame of the intact foam from step (1).
5. Populate the unmapped ligaments from the foam volume with synthetic grain structure based on characteristics of the experimentally measured data.

These steps are detailed in the following subsections.

2.1. Reconstruction of Baseline Intact Foam

A 3.4 × 3.5 × 4.7 mm^3 volume of foam was carefully machined out of a bulk batch of foam to provide a relatively large, yet tractable, volume of foam for 3D grain mapping. The sample was extracted using wire electrical discharge machining (EDM) and subsequently imaged using a Varian BIR 150/130 X-ray CT system. The scans were carried out using source voltage and current of 45 kV and 60 μA, respectively. The X-ray energy settings were chosen to provide reasonable contrast between the specimens and empty space in the reconstructed images while avoiding saturation. The source-to-detector distance was 493.7 mm and the source-to-sample distance was 170 mm. The specimen was imaged throughout a full 360° rotation, resulting in a total of 1800 transmission images. The above-mentioned parameters were selected to provide the highest possible spatial resolution that the system would allow while ensuring that the entire volume of foam remained within the field of view. The resulting voxel size was 14 μm. The Varian reconstruction software was used to produce a stack of 16-bit grayscale tomographic images. The tomographic images were segmented in Avizo®. The resulting 3D reconstruction of the foam sample serves as the baseline, to which all subsequent virtual reconstructions are mapped. Fig. 1 shows the reconstructed volume of interest.

2.2. Physical Extraction of Individual Ligaments

As mentioned previously, the beam width for HEDM measurements at the APS Sector 1-ID beamline precludes the direct measurement of the full 3.4 × 3.5 × 4.7 mm^3 sample of foam without significant investment in experimental technique development and accompanying software methodologies; thus, the next step of the experimental procedure is to physically extract individual ligaments such that they fit within the beam width throughout a full 360° rotation. A plasma focused ion beam (the FEI Helios™ PFIB DualBeam™) was selected for this mesoscale milling process due to: 1) the minimal amount of damage imparted on material surrounding the milling site and 2) the relatively fast milling time compared to a conventional FIB. Additionally, whereas the PFIB utilizes xenon for the milling, the conventional FIB utilizes gallium, which could react with the aluminum alloy's surface. For these reasons, it was determined that the PFIB would serve as an ideal mesoscale milling tool for this type of application.

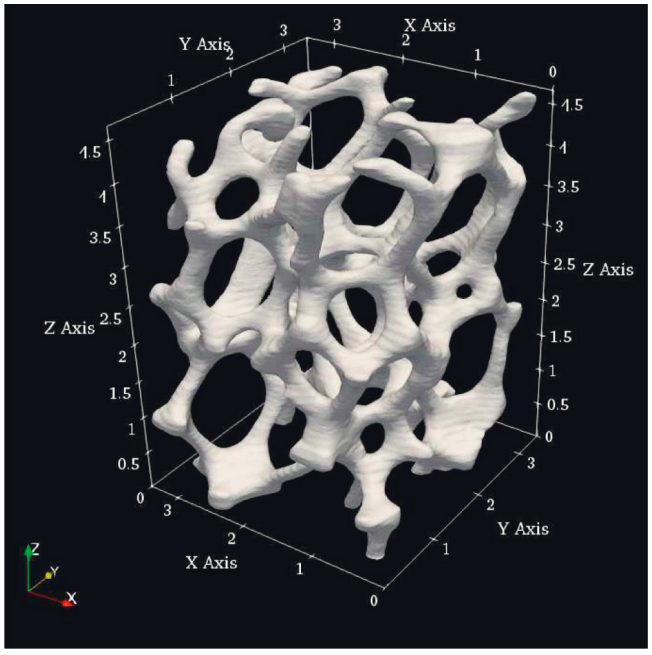

Fig. 1. X-ray computed tomography reconstruction of the sample post-EDM. Dimensions are in mm.

Prior to extracting ligaments using the PFIB, the 3D reconstruction of the sample (Fig. 1) was visualized using Paraview [32], and virtual cuts were performed to plan out the milling procedure. The planned cuts were then carried out using the PFIB with xenon at an energy of 1.3 μA. The entire cross section of a given ligament was completely milled away, unless it was the last remaining connection to the sample, in which case a small 20 μm tab of material was left to prevent the ligament from falling inside the chamber. Then, to excise the ligament, a tungsten needle with a 10 μm-diameter tip (known as an EasyLift manipulator) was adhered to the ligament by depositing a thin layer of platinum, shown in Fig. 2 (a). Once the needle was secured, the remaining tab of material was milled away and the EasyLift was retracted to excise the ligament from the sample. At the ligament surface nearest to the plasma source, the maximum amount of material affected by the milling procedure was approximately 30 μm. This amount of material loss is deemed to be insignificant, as the grains are believed to be much larger than 30 μm based on preliminary EBSD measurements [23].

Once each ligament was excised using the EasyLift, it was placed within a plastic mount (Fig. 2 (b)) before releasing the ligament from the EasyLift by milling the platinum connection. The plastic mounts were specially designed to facilitate both transportation to, and HEDM measurements at, Argonne National Laboratory. The mounts were 3D printed using ABS plastic and consist of a square base and a cylindrical well, shown in Fig. 2 (c). The well was designed to have an inner diameter less than 2 mm, such that any sample contained within it could be successfully interrogated by the X-ray beam throughout a full 360° rotation. After placing each ligament in the well of the mount, it was removed from the vacuum chamber of the PFIB DualBeam™, placed within a membrane box, and labeled. In total, ten ligaments were successfully extracted and transported to the APS at Argonne National Laboratory for grain mapping. The ten ligaments are shown in Fig. 3.

2.3. High-energy X-ray Measurements of Individual Ligaments

High-energy X-ray measurements were performed at Sector 1-ID of the APS at the 1-ID-E station. Two different types of measurements were conducted for each of the ten extracted ligaments using a beam energy of 51.996 keV, which corresponds to the K-edge of Terbium (Tb, Z = 65). First, X-ray CT measurements were made to enable reconstruction of the geometry of each ligament in the APS coordinate system, which later facilitates transforming the data to the lab-source coordinate system (described in Section 2.4). The tomography scans were conducted using a high-energy monochromatic parallel X-ray beam that illuminates a 1.8 mm wide by 1.4 mm tall region of the sample. X-ray CT images were obtained with a Retiga 4000 CCD camera that has 2048 × 2048 pixels. A 25 μm thick LuAG:Ce scintillator was used to convert transmitted X-rays to visible light, which is collected by the CCD. The native pixel size of the Retiga is 7.4 μm. A 7.5× optical objective was utilized to obtained an effective pixel size of approximately 1 μm. The CT scans were performed over a full 360° rotation in 0.2° integrations. Each exposure lasted for 0.21 s. With brightfield and darkfield image collection, the total scan time for a single layer was on the order of 10 min. Each scan resulted in a total of 1801 transmission

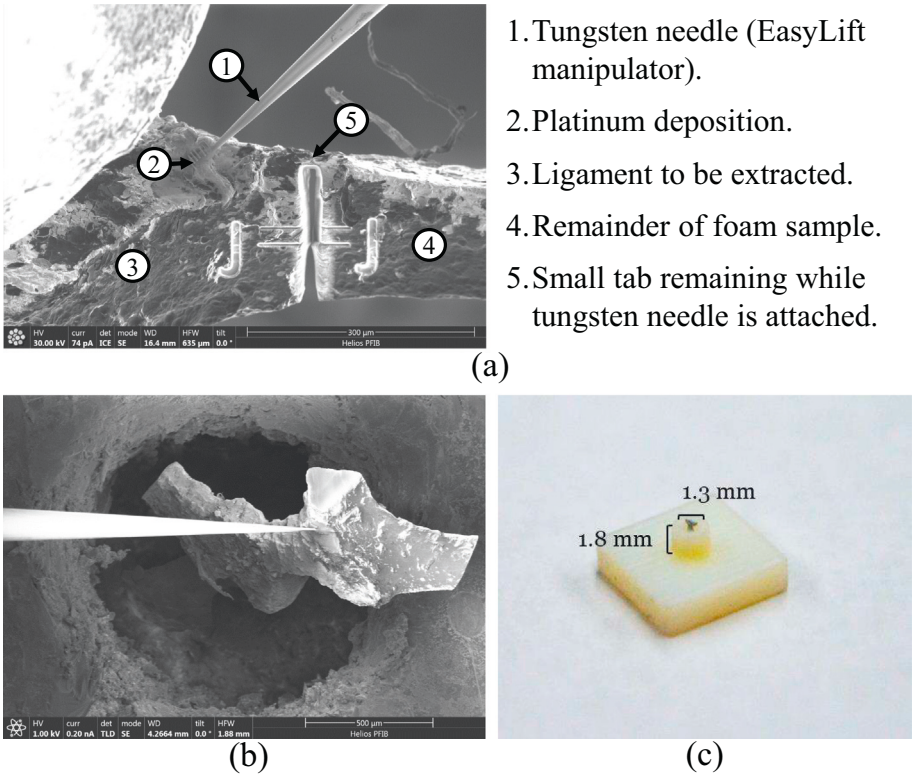

Fig. 2. (a) Micrograph taken during the ligament-extraction process for one of the ligaments. The labels imprinted on the sample are meant only for fiducial marking purposes. (b) Placement of an extracted ligament into the well of a 3D-printed plastic mount. (c) 3D-printed mount with segment of foam inside.

images that were transformed into 1801 absorption images. After the location of the rotation axis was optimized in the tomographic analysis, the data were reconstructed using a standard inverse radon transform (iradon in MATLAB [33]), resulting in a virtual stack of 1400 slices. The stack was then manually segmented, and reconstructed using Avizo®, resulting in a stereolithography (.stl) file for each scan. The tomographic reconstructions from the APS were used to ascertain the surface geometry of each ligament and facilitate registration with the baseline CT scan described in Section 2.1, rather than to extract detailed density information. Thus, there was no need for extensive artifact removal in this investigation.

During the same beam run, each ligament was measured using far-field HEDM [25-31]. A schematic of the generic far-field HEDM setup is shown in Fig. 4. The far-field HEDM measurements for each ligament were performed sequentially with the tomography measurements, using the same rotation stage and beam center that were used for the tomography scans. The high-energy X-ray beam was used to illuminate a 1.8 mm wide by 0.8 mm tall region of the sample, and diffraction spots were detected for any grains within the illuminated domain that satisfied the Bragg condition. Since the beam is monochromatic, the sample was rotated about the vertical axis to ensure that individual lattice planes in the grains were brought into the diffraction condition.

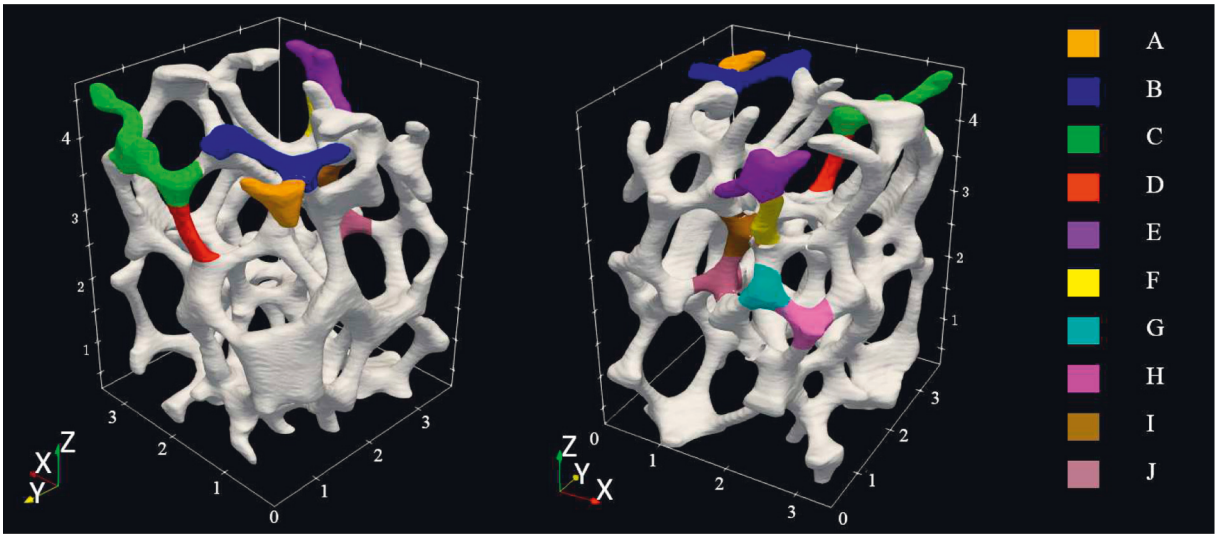

Fig. 3. Ten segments of foam (colored by ligament ID) were extracted and successfully measured. Here, two different views are depicted for the same sample shown in Fig. 1. (For interpretation of the references to color in this figure legend, the reader is referred to the web version of this article.)

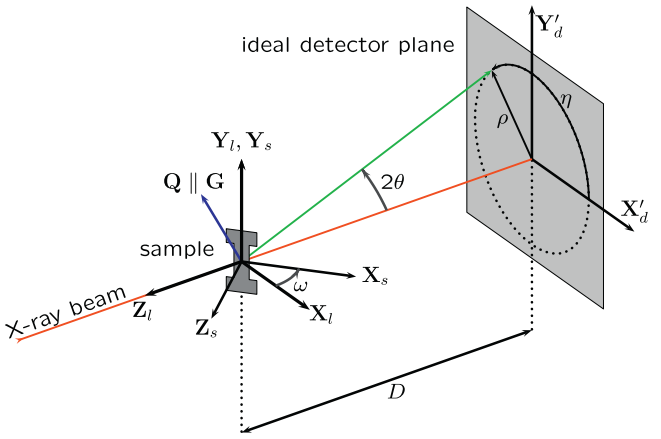

Fig. 4. Schematic of the general far-field HEDM setup showing the reference frame used in HEXRD (reprinted with permission from the publisher) [29]. For a complete description of the annotations and subscripts used in the figure, please refer to the original source.

A GE-41RT far-field area detector with 2048 × 2048 pixels was used. The pixels are square with a pixel size of 200 μm. The detector was placed 723.7 mm downstream of the rotation axis. The dynamic range of this detector is 14-bits (up to 16,384 counts) with a fairly uniform background near 1700 counts. The procedure for setting the attenuation consisted of performing small far-field diffraction scans on a single aluminum ligament while varying a combination of three different attenuators until the maximum over the integration window was sufficiently below the dynamic range of the GE detector. The integration time for each diffraction image was 0.3 s. The small scans were performed on a full 60° wedge with each diffraction image encompassing 0.25° of rotation. The small scans were then collapsed onto a single image by performing a maximum over all frames. An attenuation factor of roughly 33× was used, such that the maximum intensity for observed diffraction peaks was near 12,000 counts. This dynamic range allowed for a roughly 20× range in grain sizes to be detected. Given the largest observed grains being on the order of 500 μm, the authors are confident that all grains larger than roughly 25 μm were captured. The far-field diffraction geometry placed the X-ray beam at the center of the GE detector. The detector distance, detector size, and detector pixel size allow for full Debye-Scherrer diffraction rings up to 15.8° to be measured. Face-centered cubic aluminum with lattice parameter (a = 4.045 Å), combined with the X-ray beam energy and far-field diffraction geometry used, allowed for the measurement of diffraction rings from {111} up to {240}, with 2θ values of 5.85° and 15.15 °, respectively. All of these diffraction rings were used in the analysis with a subset from {020} to {040} used for initial orientation seeding. Each far-field HEDM scan took approximately 25 min. Ligaments B, C, and F shown in Fig. 3 were larger than the beam height, and multiple scans were necessary. Raw output from the far-field HEDM scans included grayscale images of diffraction spots collected at 0.25° increments of angular rotation, ω, over a complete 360° rotation.

The Python-based code HEXRD [29] was used to analyze the diffraction spots from the far-field HEDM measurements. HEXRD takes as input the grayscale diffraction images along with details pertaining to the experimental parameters. Standard darkfield correction was applied in the HEXRD analysis to remove the spatially varying components of the background. A threshold value of 50 counts was used for the HEXRD analysis, which was determined heuristically by looking at darkfield corrected diffraction images. Completeness values, which represent the ratios of observed Bragg reflections to those predicted by the HEXRD diffraction model, were found to be 1.0 (the highest possible value) for all but two of the indexed grains. The two exceptions had completeness values of 0.991 and 0.627, which were considered to be above the threshold considered for reliable fits (a more complete description of HEXRD's selection criterion is provided, e.g., in Ref. [34]). For this experiment, CeO_2 powder was used to calibrate the geometric parameters of the GE detector, including detector distance, beam-center position, in-plane tilts, and distortion. Z-tilt was assumed to be zero. This assumption did not negatively affect the ability to index grains. The locations of simulated diffraction spots were compared against the experimental η-ω maps. The simulated diffraction spot locations showed no systematic bias in η or ω, and further, the simulated spots accounted for nearly all of the experimentally observed diffraction spots. This indicates that the found orientations account well for the observed diffraction signal. The code outputs a text file containing centroid positions of the detected grains and the respective crystallographic orientation for each grain. The orientation of each grain is given in angle-axis representation. The grain information output from HEXRD for a given ligament is represented with respect to that ligament's local reference frame, denoted in this work as x', y', and z'.

In total, sixteen CT scans and sixteen far-field HEDM scans were completed to fully characterize all ten ligaments.

2.4. Transformation from Local Ligament Frame to Global Reference Frame

To go from the HEXRD reference frame to that of the original, intact foam (shown in Fig. 1 and denoted in this work as x, y, and z), a distinct rotation matrix, **Q**, is sought for each of the ten ligaments. To find this rotation matrix, the authors have elected to implement a relatively simple method (cf. Brannon [35]) for finding the affine mapping based on the movement of four points in space. The first step in the method is to solve for the deformation gradient tensor, **M**, such that the motion of any point on the individual ligament can be used to find the same point on the original volume. This step involves identifying several landmarks that can be collocated in the X-ray CT reconstructions from Sections 2.1 and 2.3 for a given ligament. The step-by-step procedure for finding **M** is provided in the Appendix. In general, the second-order tensor, **M**, describes both rotation and stretch. While a pure rotation matrix is sought to map each ligament from its local frame to the original (goal) frame, variance in tomography resolution and human error associated with manually selecting landmarks results in a tensor that is not orthogonal, as it should be for a pure rotation. Thus, the final step of the mapping is to perform a polar decomposition of **M** to determine the orthogonal matrix **Q** that describes the rigid-body rotation needed to return each ligament to its orientation in the original foam sample.

All rotation matrices were validated by applying them to transform the coordinates contained within the .stl files of their respective ligaments. The updated ligament configurations were then compared to the corresponding regions from the global reconstruction shown in Fig. 1. Once validated, each rotation matrix was applied to update the representation of crystal orientation of each grain within a given ligament, but only once the orientation had been converted from angle-axis to Bunge Euler convention. Essentially, this mapping updates the reference coordinate system of the Bunge Euler angles from the HEXRD reference frame to the global frame shown in Fig. 1.

Finally, the position of each grain centroid was updated from the local reference frame to the global reference frame and expressed relative to the global origin. The outcome of this step is a set of centroid coordinates and crystal orientations for each measured grain, represented in the global coordinate system of the original foam volume.

2.5. Generation of Synthetic Grain Data

The objective of the virtual reconstruction and synthetic grain mapping is to leverage the software DREAM.3D [36] to first populate regions of the foam with known grain measurements from experiment (described above), and subsequently to populate the remaining regions of foam with synthetic grain data informed by the measured grain population. DREAM.3D is a widely used software for creating digital

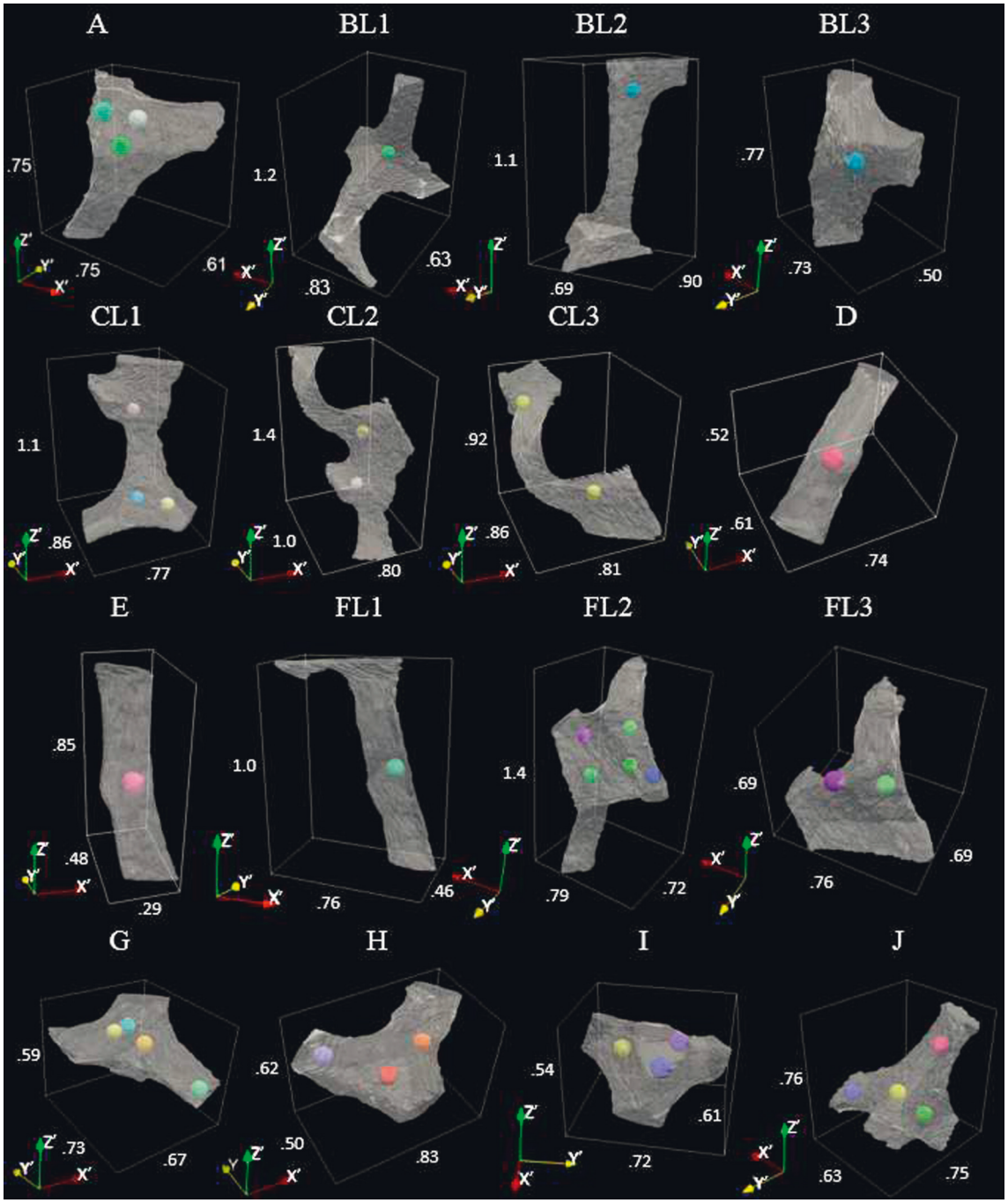

Fig. 5. Grain centroids within each ligament detected from far-field HEDM measurements. The color of each centroid corresponds to the grain's respective crystal orientation, represented with standard inverse pole figure coloring plotted with respect to the local z' direction of the corresponding ligament. Dimensions are in millimeters. (For interpretation of the references to color in this figure legend, the reader is referred to the web version of this article.)

representations of 3D microstructures using either image slices (e.g. from serial sectioning) or by instantiating microstructures based on grain-scale statistics (e.g. grain size, aspect ratio, crystallographic texture). In this work, DREAM.3D was used to instantiate a grain-mapped foam volume using microstructural quantification procedures (i.e., filters) that were layered in a sequence (i.e., pipeline). The pipeline, which is described next, was first used to approximate the grain morphologies of the measured population of grains and subsequently to quantify their characteristics (e.g., grain size). That information was then used to postulate a set of synthetic-grain centroids within the remaining unmapped volume of foam. Finally, the centroids for the measured and synthetic populations were combined, and the pipeline was again executed to map the entire volume of foam. Further details are described next, and the actual pipeline is provided in the data link at the end of this manuscript.

A general description of the DREAM.3D pipeline used in this study is provided here. The pipeline first initializes the domain of the volume. Assigned are the dimensions, resolution, and origin matching the nominal volume for the domain of interest (in this case, the baseline foam shown in Fig. 1). Next, the grain data (viz., grain-centroid coordinates and crystallographic orientations represented in Bunge Euler notation) are imported and used to seed all of the grain centers within the volume. The packing routine in DREAM.3D grows each grain in a specified shape until it impinges on another grain or on the boundary of

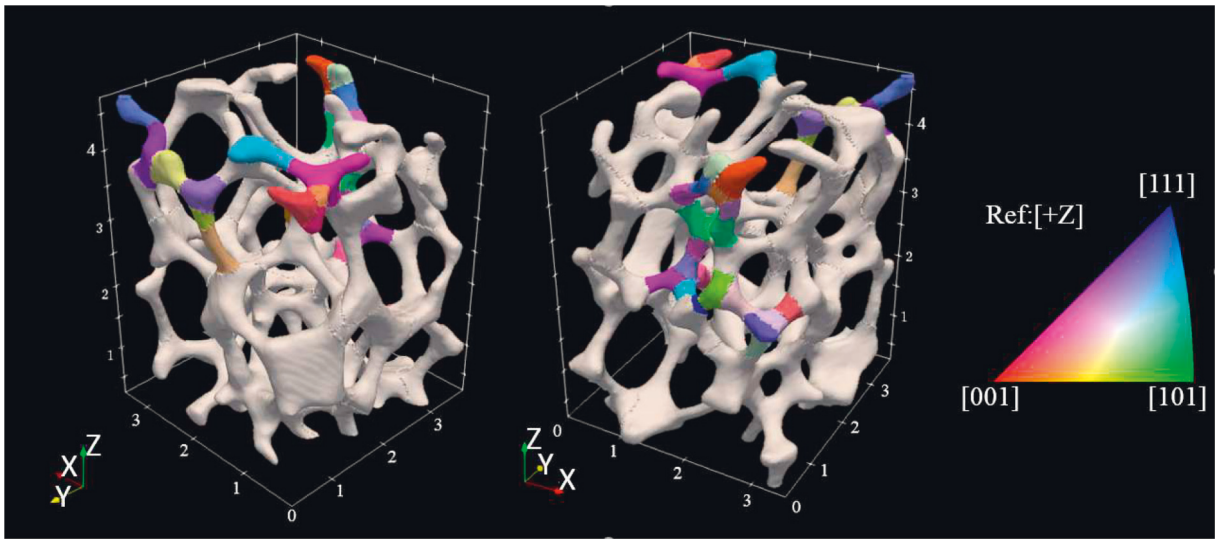

Fig. 6. 3D rendering of open-cell aluminum foam showing the ten grain-mapped ligaments (colored regions) measured using far-field HEDM. Inverse pole figure map plotted with respect to the global z direction. Here, two different views are depicted for the same sample. Dimensions are in millimeters. (For interpretation of the references to color in this figure legend, the reader is referred to the web version of this article.)

the nominal volume. In this experiment, grain growth was specified as spherical (i.e., equiaxed), as the grain shapes are unknown *a priori*. Once the packing routine has filled the nominal volume with grains, a foam "mask" is established by assigning each voxel in the domain a grayscale value as determined from the X-ray CT reconstruction of the baseline foam. A scalar threshold is applied to the grayscale values, thus establishing the mask, i.e. voxels comprising foam segmented from voxels comprising void space. The mask is then applied to the fully dense volume, resulting in a grain-mapped open-cell foam. Finally, the pipeline calculates a best-fit ellipsoid for each grain and reports the data to the user, including aspect ratios, semi-axis lengths, and orientation of each best-fit ellipsoid [36,37]. The details of the DREAM.3D synthetic builder are described in Ref. [38]. Note that this pipeline creates a grain structure based solely on the grain centers without prior knowledge of their boundaries with the surrounding grains. It is emphasized that although the packing routine is based on spherical growth, the application of the foam mask results in generally non-spherical grain shapes.

The aforementioned pipeline was first executed using the input files corresponding to the grain data derived from far-field HEDM measurements (see Section 2.4). The next step was to leverage information about the measured grains to establish centroid locations for representative, synthetic grains in the portions of the foam that were not experimentally measured. Due to the grain sizes relative to the volume of measured foam, there is not a statistically significant number of orientations detected, in this particular sample, to establish an orientation distribution function to quantify texture. Thus, only the volume of the grains (calculated using parameters from DREAM.3D's ellipsoidal fits) was used to instantiate the synthetic microstructure in this particular case. It is noted, however, that had a sufficient number of grains been detected to establish the crystallographic texture of the foam, this information could be used within DREAM.3D to inform the texture of the synthetic-grain map. This is discussed further in Section 3.

A Python script was used to generate the desired grain-information file to fully populate the foam. The script requires user input about the boundaries of the nominal volume and an initial estimate of the number of grains that should be generated. This initial estimate is simply based on the nominal, fully dense volume and the average grain volume quantified above. The script then randomly generates centroid positions within the nominal volume and crystal orientations for the specified number of grains to populate the nominal, fully dense volume. It then imports centroid information from the measured population and eliminates spatially conflicting synthetic grains. A data file containing both measured- and synthetic-grain information (i.e. centroid coordinates and crystal orientations) is then written out and imported into DREAM.3D. The previously described pipeline is again executed to produce a synthetic/measured grain-mapped foam. The average grain size is computed based on best-fit ellipsoids for the entire population of grains and compared to that of the measured population. If necessary, the initial estimate for the number of grains with which to seed the nominal volume is updated, and the process is repeated until the average grain size of the entire population falls within 1% of that for the measured population. For the foam sample studied here, this was achieved by randomly generating an initial list of 525 grain centroids, concatenating the list with the measured grain centroids, and eliminating any of the synthetic centroids that conflict spatially with the measured centroids. The updated list was then input into the DREAM.3D pipeline. More details regarding the final results, after applying the foam mask, are provided in the next section.

3. Results and Discussion

Fig. 5 shows the locations of grain centroids superimposed on a tomographic reconstruction of each of the ten extracted ligaments based on the high-energy X-ray measurements performed at the APS 1-ID beamline. The "L" in the label of ligaments B, C, and F denotes one layer in a multi-layer scan for a single sample, e.g. "BL1" is the first scan layer of ligament B shown in Fig. 3. Each ligament shown in Fig. 5 is depicted with its local coordinate system (x', y', z'), which is referenced by HEXRD. The color of each sphere represents the crystallographic orientation of the respective grain, plotted in conventional inverse pole figure (IPF) color space relative to the local z' direction.

The reconstructed foam volume and the grain-mapped ligaments that were measured in experiment are provided in Fig. 6. Based on the reconstructions from far-field HEDM, a total of 32 grains were measured among the ten extracted ligaments. The color of each grain-mapped region corresponds to the crystal orientation, represented using an IPF color map plotted with respect to the vertical (z) direction of the global reference frame. Each color represents a different grain that was detected using the far-field HEDM measurements. If two scan layers of the same section resulted in the same grain found, the two grains were resolved into one by averaging the centroid's location. Based on DREAM.3D's best-fit ellipsoids of the reconstructed measured grains (described in Section 2.5), the average aspect ratios were $b/a = 0.644$ and $c/a = 0.492$, where a, b, and c are the semi-axis lengths of the

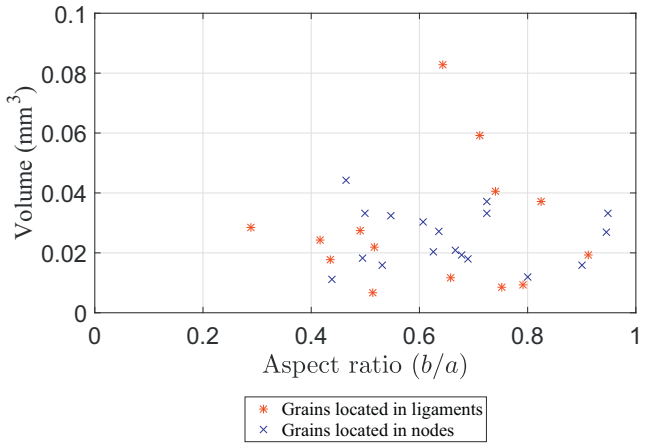

Fig. 7. Grain size (based on ellipsoidal best fits) versus aspect ratio for all 32 measured grains.

ellipsoid in decreasing order. The average semi-major-axis length was found to be 274 μm, which is quite large relative to the size of ligaments within the foam. In some cases, single grains are shown to occupy entire ligaments. This corroborates the limited two-dimensional data existing in the literature [15,17,18]. Given that the grain size is large relative to the dominant structural feature (i.e. ligament), the authors hypothesize that the local deformation response will be sensitive to the underlying grain structure. Testing this hypothesis is beyond the scope of the current work and will be addressed in a future study.

A plot displaying the ellipsoidal volume versus aspect ratio (b/a) for each of the 32 measured grains can be seen in Fig. 7. The results shown in Fig. 7 indicate that the majority of grains are non-spherical, despite being formed from a spherical packing routine. The reason for this is that, as described in Section 2.5, the packing routine is applied to populate a nominal, fully dense volume. Once the foam mask is subsequently applied, a non-spherical shape is imparted on the grains that remain within the foam volume. The results shown in Fig. 7 also indicate that, among the 32 measured grains, those grains located within ligaments appear to have a wider range of sizes and aspect ratios as compared to grains located within nodes. During the actual solidification process, grain growth within a ligament is physically constrained by the dimensions of that particular ligament. As a result, intra-ligament grain growth has fewer degrees of freedom compared to grain growth within a node, where grains are likely able to grow in a more isotropic (i.e., equiaxed) manner. Consistent with this explanation, Fig. 7 shows that the grain with the lowest aspect ratio resides in a ligament, while the grain with the highest aspect ratio (closest to one) resides in a node. The authors note that more data should be collected to determine the statistical significance of this apparent trend.

As previously indicated, there are too few data points contained within the measured population to substantiate any claims about crystallographic texture of a larger volume of foam. Efforts are underway to improve efficiency of the measurement method, which would enable experimental characterization of larger volumes of the open-cell foam. Alternatively, other methods (including powder diffraction and neutron diffraction) could be used to complement the method presented here by providing more conclusive evidence regarding the crystallographic texture of the foams and to explore, for example, the impact of various heat treatments.

Fig. 8 provides a visualization of the grain-mapped foam that contains the grains mapped from experiment (shown in Fig. 6) integrated with synthetically generated grains to populate the remaining foam volume. Following augmentation with synthetic data, the total number of grains in the fully grain-mapped foam sample shown in Fig. 8 is 264.

3.1. Sources of Error and Variability

Several sources of error and variability arise throughout the grain-mapping procedure, which impact the final 3D grain map of the foam. Experimental error associated with the far-field HEDM measurements is deemed to be a relatively insignificant source of error for the sample studied in this work. This assessment is based on the completeness measures that were reported in Section 2.3, which were found to be well within the range of acceptability for grain indexing. Error associated with identifying the rotation matrices (Section 2.4) is also deemed to be a relatively insignificant source of error in the overall methodology. As described in Section 2.4, each of the rotation matrices was validated by transforming the reconstructed CT data for each ligament measured at the APS (Section 2.3) and comparing the result to the baseline CT reconstruction of the foam described in Section 2.1. Ultimately, these rotation matrices were used only to update the reference frame of the Euler angles for each grain detected through HEXRD. Since the geometry of the final grain-mapped foam was based on the original baseline CT measurement, there is no error in the geometrical representation of the foam associated with the rotation matrices.

A more significant source of error arises during the packing procedure described in Section 2.5. Recall, the far-field HEDM technique used in this work provides only the centroids of detected grains and does not explicitly resolve grain morphologies (hence, grain boundaries). Rather, the grain boundaries are approximated by applying the routines described in Section 2.5. Thus, discrepancy is expected to result between the actual and approximated grain boundaries within the ligaments. While it is difficult to provide a quantitative measure of this error (as there is not a complete mapping of the known grain boundaries within the ligaments), the authors have attempted to provide a qualitative comparison for one of the ligaments in which some of the grain boundaries are known. In Fig. 9, the cross section of ligament I is shown through a sequence of image slices that are spaced 12 μm apart. Fig. 9 (a) shows the image slices based on the high-resolution X-ray CT data collected at the APS. As shown in Fig. 9 (a), semi-continuous strings of precipitates decorate portions of the grain boundaries, which was similarly observed in Refs. [15,16]. Fig. 9 (b) shows the corresponding slices from the 3D grain map of the virtually reconstructed foam from Fig. 6. Within the cross-sections shown in Fig. 9 (b), the approximated grain boundaries are depicted by solid lines, and the known grain boundaries (traced from Fig. 9 (a)) are depicted by dashed lines for reference. While the approximated grain boundaries do not line up precisely with the actual grain boundaries, there are visible similarities between them. In both cases, the grain boundaries suggest a bamboo-like grain structure within the ligaments. It is certainly worth investigating the implications of grain-boundary-approximation error in terms of modeling outcomes, but such an investigation is beyond the scope of this work. Improvements in the grain-boundary representation could be made by using alternative measurement techniques that are capable of non-destructively mapping grain morphologies. These included, for example, near-field HEDM [30,39-42], which is generally more time consuming than far-field HEDM.

Another potential source of error in the grain-mapping procedure is the generation of synthetic grain structure, described in Section 2.5. Unfortunately, it is not possible to quantify this error, given that the microstructure is unknown in regions that were synthetically grain mapped. However, the authors have performed an investigation to quantify the variability in the microstructural statistics caused by randomly seeding grain centroids during the synthetic grain-mapping procedure. The purpose of this study is to provide the reader with a sense of the variability that can be expected to occur among different instantiations of the same grain-mapped volume. To conduct the study, nine additional foam instantiations were created by randomly generating a list of 525 grain centroids; concatenating the list with the 32 measured grain centroids; removing any conflicting centroids from the

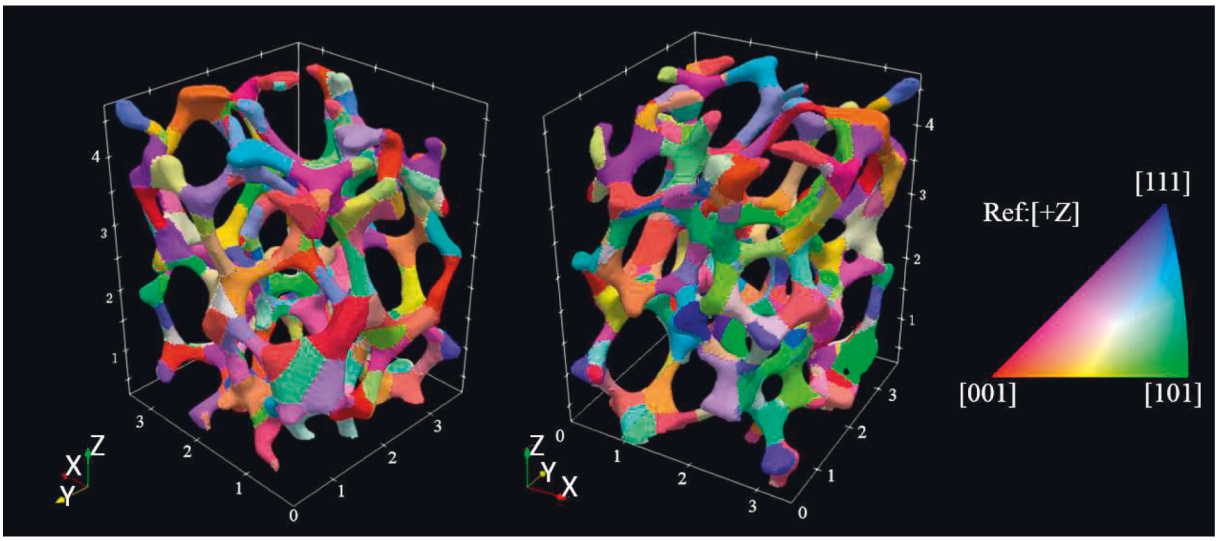

Fig. 8. 3D rendering of grain-mapped, open-cell aluminum foam after integrating measured and synthetic data. Inverse pole figure map plotted with respect to the global z direction. Here, two different views are depicted for the same sample. Dimensions are in millimeters.

population of synthetic grains; and inputting the new list of grain centroids, along with the X-ray CT data for the baseline foam, into the pipeline described in Section 2.5. For each of the ten instantiations (including the original one reported above and shown in Fig. 8), a distribution was fit to the entire population of grains (both synthetic and measured) in the grain-mapped foam for each of the following parameters: aspect ratio (b/a), semi-major-axis length, and ellipsoidal volume. The best-fit distributions were found using MATLAB's built-in fitdist function. For aspect ratio and semi-major-axis length, Gaussian distributions were found to provide the best fit; while an exponential distribution was found to provide the best fit for ellipsoidal volume of the grains. Based on the distributions for each foam instantiation, an average (μ) and standard deviation (σ) were calculated. Note that for the exponential distribution, μ and σ are equivalent. Then, to quantify the differences among the ten instantiations, the relative error was calculated for both the μ and σ values for the three grain measures, as follows:

$$e_\mu = \sqrt{\sum_{i=1}^{10}\left(\frac{\mu_i - \overline{\mu}}{\overline{\mu}}\right)^2} \tag{1}$$

$$e_\sigma = \sqrt{\sum_{i=1}^{10}\left(\frac{\sigma_i - \overline{\sigma}}{\overline{\sigma}}\right)^2} \tag{2}$$

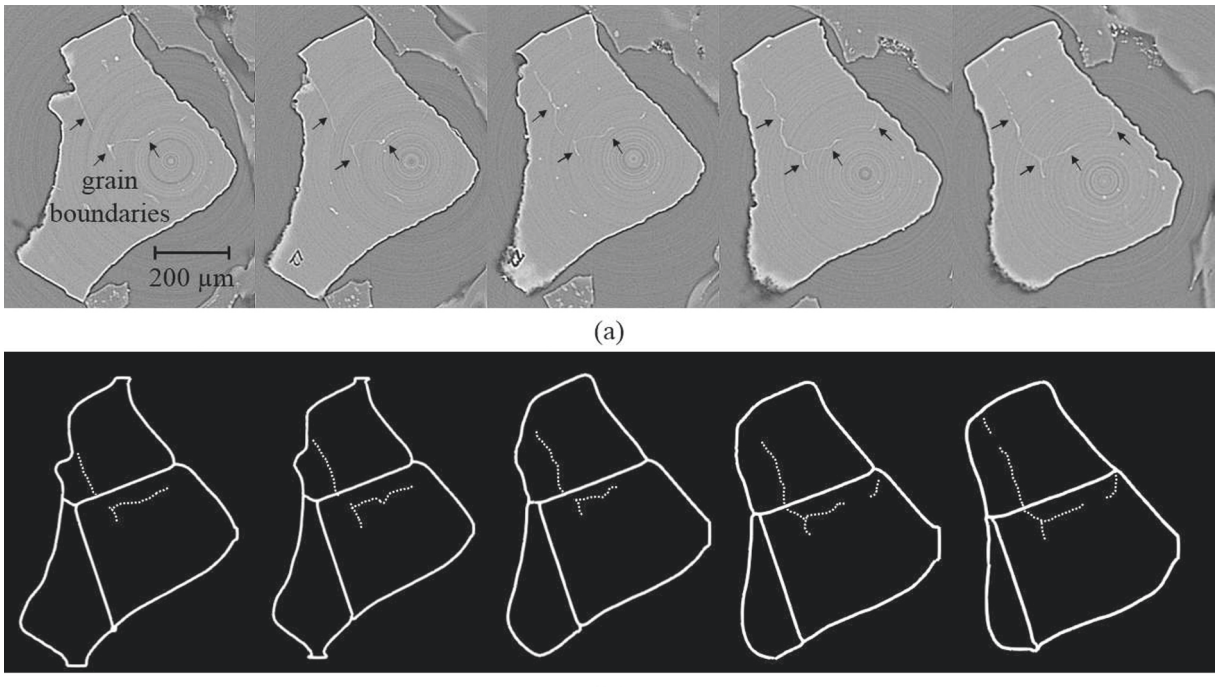

Fig. 9. (a) Tomography slices of a single ligament with precipitates along the grain boundaries highlighted. (b) Corresponding slices from the virtual reconstruction of the grain-mapped foam shown in Fig. 6. Within the cross section, solid lines indicate the approximated grain boundaries, and dashed lines indicate the known grain boundaries traced from (a).

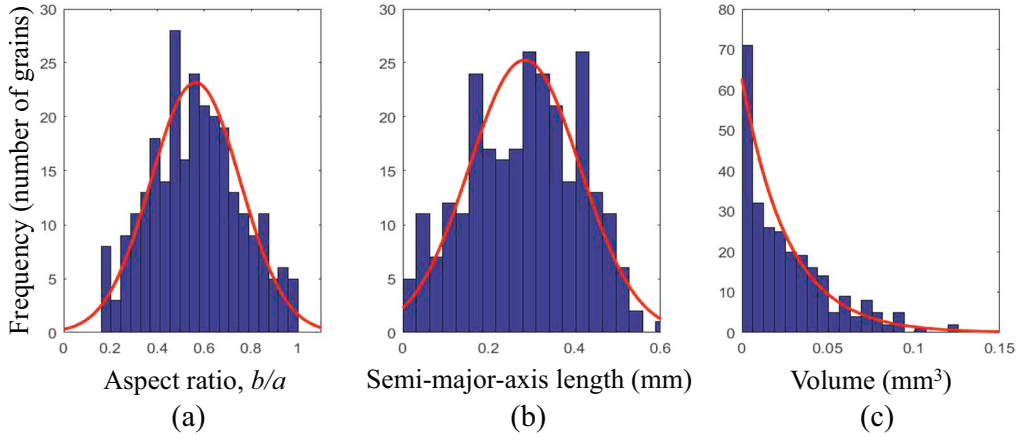

Grain characteristic*	μ of measured population (N=32)	μ of original instantiation (N=264)	$\bar{\mu}$ of all 10 instantiations (N=2673)	$\bar{\sigma}$ of all 10 instantiations (N=2673)	e_μ (%)	e_σ (%)
Aspect ratio (*b/a*)	0.644	0.563	0.559	0.186	4.49	10.48
Semi-major-axis length	0.274 mm	0.284 mm	0.285 mm	0.126 mm	8.87	7.51
Volume	0.0264 mm³	0.0265 mm³	0.0261 mm³	0.0261 mm³	12.46	12.46

*Based on best-fit ellipsoid from DREAM.3D

(d)

Fig. 10. (a) Histogram of aspect ratios (*b/a*) for the entire population of grains in the original instantiation of foam shown in Fig. 8. The histogram is also plotted with a curve that represents the best-fit Gaussian distribution. (b) Histogram of semi-major-axis lengths for the entire population of grains in the original instantiation of foam shown in Fig. 8, plotted with a best-fit Gaussian distribution. (c) Histogram of volumes of best-fit ellipsoids for entire population of grains in the original instantiation of foam shown in Fig. 8, plotted with a best-fit exponential distribution. (d) Table of averages, standard deviations and relative errors for the aspect ratios (*b/a*), semi-major-axis lengths, and ellipsoidal volumes reported from DREAM.3D.

where μ_i and σ_i denote the average and standard deviation, respectively, of the *i*th instantiation, and $\bar{\mu}$ and $\bar{\sigma}$ represent the averages of μ and σ, respectively, over all ten instantiations. The results from this analysis can be seen in Fig. 10. Recall that the original foam instantiation was created by ensuring that the average grain size (based on volume) was within 1% of that for the measured population, which is evident by comparing the average volumes in the table provided in Fig. 10. The average semi-major-axis length of the grains in the original foam instantiation is approximately 3.6% larger than that of the measured population. Interestingly, the average aspect ratio of the grains in the original foam instantiation is 12.6% smaller (more elliptical) than that of the measured population of grains. This disparity in aspect ratio is attributed to two likely sources. The first has to do with how the packing routine handled grains from the measured population that were near the FIB-milled boundaries. Specifically, those grains that impinged on the boundary of an adjacent ligament that had not been measured using HEDM were truncated at that boundary, which would generally result in less elongated grains. Consequently, the average aspect ratio among the measured population of grains could be skewed slightly due to this truncation effect. The second likely source of disparity between the average aspect ratios could be a side effect of the synthetic generation of grain centroids being unconstrained to the geometry of the foam. As mentioned previously, the synthetic grain centroids are randomly assigned throughout the nominal volume of the sample, including void space. It is likely that many grains whose centroids belong to the void space become preferentially elongated with ligaments once the foam mask is applied. Considering the entire population of synthetic grains, this effect could serve to decrease the overall average aspect ratio as compared to the measured population. This observation appears to be systematic, as the reported relative error for the average grain aspect ratio is low considering all ten instantiations. The accuracy of the grain aspect ratios could be improved by incorporating a grain-growth algorithm that better represents the physics of the investment-casting process and also by collecting more grain measurements from experiment, ideally for a bulk sample of foam. Overall, the analysis presented here provides a measure of the variability in the distributions of grain size and shape parameters caused by the synthetic-grain generation process.

3.2. Discussion of Method

As described in Section 1, characterizing the grain structure for a meaningful volume of ultra-low-density metallic foam is non-trivial due to the sparse and fragile network of ligaments, or struts. Serial sectioning techniques [43-47] are not well suited for this type of cellular structure because of the sparsity of material, in which case EBSD data would yield useful information for only a small percentage of a nominal cross section. Further, serial-sectioning methods are destructive and would not allow further measurements or testing of the material. While the method presented here of excising individual ligaments does preclude subsequent mechanical testing of the bulk sample of foam, the individual ligaments remain intact after the HEDM measurements and can still be mechanically tested, similar to the ligament-scale testing that was carried out by Zhou et al. [16]. In that work, the mechanical properties of individual ligaments were found to be significantly different than those of the same bulk alloy, and Zhou et al. attributed the observed difference to unique grain structures within the ligaments (although, the grain structure was not quantitatively measured in their work).

A limitation of the experimental procedure described here is the required access to a synchrotron-source with HEDM capability. The number of ligaments that can be measured using HEDM depends upon both a successful beam-time allocation and the amount of beam-time awarded for a given allocation. Although grain mapping ten ligaments using far-field HEDM is considered significant, that number still represents a relatively small portion of the original foam sample. Potential alternatives for the future would be to use a Lab-DCT system [48], which eliminates the need for access to a synchrotron facility, or a high-throughput capability at an existing HEDM (or 3D X-ray diffraction) beamline, which is an active area of development in the

community. As HEDM techniques become more accessible in the future, this particular limitation will be largely mitigated.

Another limitation of the method is the tedious nature of extracting individual ligaments. It is noted that efforts are underway to facilitate non-destructive grain mapping of relatively large volumes of foam without the need to excise individual ligaments. Such capability requires non-trivial modifications to the experimental setup and data-reconstruction algorithms, but could have significant impacts on the efficiency and throughput of data collected for open-cell metallic foams. With possible future improvements that could enable non-destructive measurements of "bulk" samples of foam (say, 5 mm diameter), it will likely still be of interest to augment the experimental data with synthetic data to represent even larger and more representative volumes of foam. In that case, rather than excising individual ligaments, one would simply excise a subvolume of foam, and the remaining methodology would be identical to that presented here.

This work represents a first step toward integrating non-destructive measurement techniques with synthetic-data generation to digitally represent fairly complex structural materials, namely open-cell metal foams. The method presented here induces some approximation, as discussed previously, but relies on information from the measured grain population to essentially expand the grain mapping over a larger volume. In general, the concept of generating multimodal data sets by integrating experimentally measured and synthetic populations could have important implications in data-driven materials design, beyond application to open-cell metallic foams. Furthermore, the ability to generate 3D grain maps of open-cell metal foams will allow for higher fidelity modeling and will enable parametric studies of the foams through virtual testing.

To the authors' knowledge, the results presented here represent the first time that the 3D grain structure, including crystallography, has been mapped and digitally represented for an open-cell metallic foam. This is significant in that such a mapping is a critical step toward investigating relationships among manufacturing/process parameters, microstructure, and mechanical behavior across multiple length scales of such foams. Overall, the integration of measured and synthetic grain maps also provides important information that can be used for grain-resolved numerical simulations of a meaningful volume of investment-cast foam.

4. Conclusions

A three-dimensional grain map is generated for an investment-cast, open-cell aluminum foam by integrating experimentally- and synthetically-derived data. The method relies on experimental measurements using far-field high-energy X-ray diffraction microscopy (HEDM) to map the grain centroids and crystal orientations within individual ligaments of the foam. Because the ligament spacing is nearly as large as the width of the X-ray beam used for the HEDM measurements, an intact sample of foam cannot be measured directly. Thus, the foam is first deconstructed by excising individual ligaments and performing the HEDM measurements on each ligament separately. The foam is then virtually reconstructed by mapping the grain data from each of the measured ligaments to the original foam volume using an affine transformation based on landmarks that can be collocated in X-ray computed tomography reconstructions in both the local, ligament reference frame and the global reference frame. In total, ten ligaments (which represent a subset of the original foam volume) were grain mapped based on the HEDM measurements. Grain information from the experimental data was then leveraged to populate the remaining regions of the foam with synthetically generated grain structure using the software, DREAM.3D. The final result is a fully grain-mapped volume of open-cell aluminum foam, which, to the authors' knowledge, is the first of its kind.

In total, there were 32 grains detected among the ten experimentally measured ligaments. In many cases, single grains span entire ligaments. The final volume of foam with integrated experimental and synthetic data consists of 264 grains. An analysis is performed to assess the variability in grain-scale statistics by generating multiple instantiations of the synthetic/measured volume of foam.

Due to the grain size relative to the ligament size, the authors postulate that the investment-cast foam studied here could exhibit size effects. That is, the local deformation mode is likely sensitive to the particular arrangement of grains within a given ligament. Testing this is beyond the scope of the current work. The method and the results presented here could have an impact on future modeling studies and efforts to link process parameters, material structure, and properties of open-cell metal foams.

Data availability

The raw and processed data required to reproduce these findings are available to download from:
http://hdl.handle.net/11256/975.

Acknowledgments

This material is based upon work supported by the National Science Foundation (DMREF-1629660), and by funding from the Undergraduate Research Opportunities Program (UROP) at the University of Utah awarded to Jayden Plumb. This research used resources of the Advanced Photon Source (APS), a U.S. Department of Energy (DOE) Office of Science User Facility operated for the DOE Office of Science by Argonne National Laboratory under Contract No. DE-AC02-06CH11357. The measurements performed at the APS Sector 1-ID beamline were associated with General User Proposal GUP-46871. This work was performed under the auspices of the U.S. Department of Energy by Lawrence Livermore National Laboratory under Contract DE-AC52-07NA27344. The authors appreciate the support of the staff and facilities that made this work possible, including Drs. Peter Kenesei and J.-S. Park of the APS, Drs. Nathan Barton and Joel Bernier of Lawrence Livermore National Laboratory, and Drs. Ted Tessner and Lee Pullan of Thermo Fisher Scientific (formerly FEI Company).

Appendix A

A full description of the method used to solve for the deformation gradient tensor, **M**, is provided here. The tensor **M**, is sought to describe the deformation and rotation between two vectors, $\vec{v}$ and $\vec{v'}$, such that:

$$\vec{v} = \mathbf{M}\cdot\vec{v'} + \vec{b}, \tag{3}$$

which is a 3D analog of the point-slope formula in two dimensions. To do this, three landmarks are selected that can be collocated in the X-ray CT reconstructions from Sections 2.1 and 2.3 for a given ligament. The first set of three points ($\overrightarrow{p_1'}$, $\overrightarrow{p_2'}$, and $\overrightarrow{p_3'}$) corresponds to the landmark locations on the ligament in its local orientation and is used to create two vectors:

$$\overrightarrow{v_1'} = \overrightarrow{p_2'} - \overrightarrow{p_1'} \tag{4}$$

$$\overrightarrow{v_2'} = \overrightarrow{p_3'} - \overrightarrow{p_1'} \tag{5}$$

that uniquely define its orientation. The second set of three points ($\overrightarrow{p_1}$, $\overrightarrow{p_2}$, and $\overrightarrow{p_3}$) corresponds to the locations of the same landmarks, but found in the original orientation, and is used to create two vectors:

$$\overrightarrow{v_1} = \overrightarrow{p_2} - \overrightarrow{p_1} \tag{6}$$

$$\overrightarrow{v_2} = \overrightarrow{p_3} - \overrightarrow{p_1} \tag{7}$$

that uniquely represent the goal orientation. These vectors are assumed to undergo rigid-body rotation only, in which case only three points (or two vectors) are required to uniquely define the rotation. However, in keeping with Brannon's more generalized approach for finding the total deformation gradient tensor based on four points, a third vector is calculated simply based on the cross product of the previous two:

$$\overrightarrow{v_3'} = \overrightarrow{v_1'} \times \overrightarrow{v_2'} \tag{8}$$

$$\overrightarrow{v_3} = \overrightarrow{v_1} \times \overrightarrow{v_2}. \tag{9}$$

The vectors are then organized into 3 × 3 matrices as follows:

$$\mathbf{V}' = [\overrightarrow{v_1'}, \overrightarrow{v_2'}, \overrightarrow{v_3'}]^T \tag{10}$$

$$\mathbf{V} = [\overrightarrow{v_1}, \overrightarrow{v_2}, \overrightarrow{v_3}]^T. \tag{11}$$

M can then be solved for using the following equation:

$$\mathbf{M} = \mathbf{V}\cdot(\mathbf{V}')^{-1}. \tag{12}$$

Note, only the rotation matrix is sought at this point, so the translation vector, $\overrightarrow{b}$, is ignored. Once the deformation gradient tensor is known, a polar decomposition can be conducted to determine the pure rotation tensor, **Q**.

References

[1] L.J. Gibson, M.F. Ashby, Cellular Solids: Structure and Properties, Cambridge University Press, 1999.
[2] A.G. Evans, J. Hutchinson, M. Ashby, Multifunctionality of cellular metal systems, Prog. Mater. Sci. 43 (3) (1998) 171–221.
[3] J. Banhart, Manufacture, characterisation and application of cellular metals and metal foams, Prog. Mater. Sci. 46 (6) (2001) 559–632.
[4] J. Banhart, Aluminum foams: on the road to real applications, MRS Bull. 28 (04) (2003) 290–295.
[5] C.-Y. Zhao, W. Lu, Y. Tian, Heat transfer enhancement for thermal energy storage using metal foams embedded within phase change materials (PCMs), Sol. Energy 84 (8) (2010) 1402–1412.
[6] R. Singh, P. Lee, R. Dashwood, T. Lindley, Titanium foams for biomedical applications: a review, Mater. Technol. 25 (3-4) (2010) 127–136.
[7] L. Murr, S. Gaytan, F. Medina, H. Lopez, E. Martinez, B. Machado, D. Hernandez, L. Martinez, M. Lopez, R. Wicker, et al., Next-generation biomedical implants using additive manufacturing of complex, cellular and functional mesh arrays, Philos. Trans. R. Soc. Lond. A 368 (1917) (2010) 1999–2032.
[8] L.E. Murr, S.M. Gaytan, E. Martinez, F. Medina, R.B. Wicker, Next generation orthopaedic implants by additive manufacturing using electron beam melting, Int. J. Biomater. (2012).
[9] L. Gong, S. Kyriakides, W.-Y. Jang, Compressive response of open-cell foams. Part I: morphology and elastic properties, Int. J. Solids Struct. 42 (5) (2005) 1355–1379.
[10] L. Gong, S. Kyriakides, Compressive response of open cell foams Part II: initiation and evolution of crushing, Int. J. Solids Struct. 42 (5) (2005) 1381–1399.
[11] C. Perrot, R. Panneton, X. Olny, Periodic unit cell reconstruction of porous media: application to open-cell aluminum foams, J. Appl. Phys. 101 (11) (2007) 113538.
[12] W.-Y. Jang, A.M. Kraynik, S. Kyriakides, On the microstructure of open-cell foams and its effect on elastic properties, Int. J. Solids Struct. 45 (7) (2008) 1845–1875.
[13] W.-Y. Jang, S. Kyriakides, On the crushing of aluminum open-cell foams: part I. Experiments, Int. J. Solids Struct. 46 (3) (2009) 617–634.
[14] K. Mader, R. Mokso, C. Raufaste, B. Dollet, S. Santucci, J. Lambert, M. Stampanoni, Quantitative 3D characterization of cellular materials: segmentation and morphology of foam, Colloids Surf. A Physicochem. Eng. Asp. 415 (2012) 230–238.
[15] J. Zhou, C. Mercer, W. Soboyejo, An investigation of the microstructure and strength of open-cell 6101 aluminum foams, Metall. Mater. Trans. A 33 (5) (2002) 1413–1427.
[16] J. Zhou, S. Allameh, W. Soboyejo, Microscale testing of the strut in open cell aluminum foams, J. Mater. Sci. 40 (2) (2005) 429–439.
[17] T. Nieh, K. Higashi, J. Wadsworth, Effect of cell morphology on the compressive properties of open-cell aluminum foams, Mater. Sci. Eng. A 283 (1) (2000) 105–110, https://doi.org/10.1016/S0921-5093(00)00623-7.
[18] E. Amsterdam, P. Onck, J.T.M. De Hosson, Fracture and microstructure of open cell aluminum foam, J. Mater. Sci. 40 (22) (2005) 5813–5819.
[19] B.V. Krishna, S. Bose, A. Bandyopadhyay, Strength of open-cell 6101 aluminum foams under free and constrained compression, Mater. Sci. Eng. A 452 (Supplement C) (2007) 178–188, https://doi.org/10.1016/j.msea.2006.10.080.
[20] S. Fischer, P. Schüler, C. Fleck, A. Bührig-Polaczek, Influence of the casting and mould temperatures on the (micro) structure and compression behaviour of investment-cast open-pore aluminium foams, Acta Mater. 61 (14) (2013) 5152–5161.
[21] V. Goussery, Y. Bienvenu, S. Forest, A.-F. Gourgues, C. Colin, J.-D. Bartout, Grain size effects on the mechanical behavior of open-cell nickel foams, Adv. Eng. Mater. 6 (6) (2004) 432–439.
[22] A. Jung, S. Diebels, A. Koblischka-Veneva, J. Schmauch, A. Barnoush, M.R. Koblischka, Microstructural analysis of electrochemical coated open-cell metal foams by EBSD and nanoindentation, Adv. Eng. Mater. 16 (1) (2014) 15–20.
[23] K.E. Matheson, K.K. Cross, M.M. Nowell, A.D. Spear, A multiscale comparison of stochastic open-cell aluminum foam produced via conventional and additive-manufacturing routes, Mater. Sci. Eng. A 707 (2017) 181–192, https://doi.org/10.1016/j.msea.2017.08.102.
[24] L.J. Gibson, M.F. Ashby, The mechanics of three-dimensional cellular materials, Proceedings of the Royal Society of London A: Mathematical, Physical and Engineering Sciences, vol. 382, The Royal Society, 1982, pp. 43–59.
[25] H.F. Poulsen, S.F. Nielsen, E.M. Lauridsen, S. Schmidt, R.M. Suter, U. Lienert, L. Margulies, T. Lorentzen, D. Juul Jensen, Three-dimensional maps of grain boundaries and the stress state of individual grains in polycrystals and powders, J. Appl. Crystallogr. 34 (6) (2001) 751–756, https://doi.org/10.1107/S0021889801014273.
[26] L. Margulies, T. Lorentzen, H. Poulsen, T. Leffers, Strain tensor development in a single grain in the bulk of a polycrystal under loading, Acta Mater. 50 (7) (2002) 1771–1779 http://www.sciencedirect.com/science/article/pii/S1359645402000289https://doi.org/10.1016/S1359-6454(02)00028-9.
[27] J. Oddershede, S. Schmidt, H.F. Poulsen, H.O. Sørensen, J. Wright, W. Reimers, Determining grain resolved stresses in polycrystalline materials using three-dimensional X-ray diffraction, J. Appl. Crystallogr. 43 (3) (2010) 539–549, https://doi.org/10.1107/S0021889810012963.
[28] J. Bernier, N. Barton, M. Brandes, U. Lienert, M. Miller, M. Mills, Exploring Crystal Plasticity Via Far-field 3DXRD, Tech. rep. Lawrence Livermore National Laboratory (LLNL), Livermore, CA, 2010.
[29] J. Bernier, N. Barton, U. Lienert, M. Miller, Far-field high-energy diffraction microscopy: a tool for intergranular orientation and strain analysis, J. Strain Anal. Eng. Des. 46 (7) (2011) 527–547.
[30] U. Lienert, S. Li, C. Hefferan, J. Lind, R. Suter, J. Bernier, N. Barton, M. Brandes, M. Mills, M. Miller, et al., High-energy diffraction microscopy at the advanced photon source, JOM J. Miner. Met. Mater. Soc. 63 (7) (2011) 70–77.
[31] J.-S. Park, J. Okasinski, K. Chatterjee, Y. Chen, J. Almer, Non-destructive characterization of engineering materials using high-energy X-rays at the advanced photon source, Synchrotron Radiat. News 30 (3) (2017) 9–16, https://doi.org/10.1080/08940886.2017.1316125.
[32] J. Ahrens, B. Geveci, C. Law, Paraview: An End-user Tool for Large Data Visualization, The Visualization Handbook, 717 (2005).
[33] MATLAB User's Guide, 5 The Mathworks Inc., Natick, MA, 1998, p. 333.
[34] V. Tari, R.A. Lebensohn, R. Pokharel, T.J. Turner, P.A. Shade, J.V. Bernier, A.D. Rollett, Validation of micro-mechanical FFT-based simulations using high energy diffraction microscopy on Ti-7Al, Acta Mater. 154 (2018) 275.
[35] R.M. Brannon, Rotation, Reflection, and Frame Changes: Orthogonal Tensors in Computational Engineering Mechanics, vol. 1, IOP Publishing, 2018, https://doi.org/10.1088/978-0-7503-1454-1.

[36] M.A. Groeber, M.A. Jackson, DREAM.3D: a digital representation environment for the analysis of microstructure in 3D, Integr. Mater. Manufactur. Innov. 3 (1) (2014) 5.
[37] M. Groeber, S. Ghosh, M.D. Uchic, D.M. Dimiduk, A framework for automated analysis and simulation of 3D polycrystalline microstructures.: Part 1: statistical characterization, Acta Mater. 56 (6) (2008) 1257–1273.
[38] J.C. Tucker, L.H. Chan, G.S. Rohrer, M.A. Groeber, A.D. Rollett, Tail departure of log-normal grain size distributions in synthetic three-dimensional microstructures, Metall. Mater. Trans. A 43 (8) (2012) 2810–2822.
[39] R. Suter, D. Hennessy, C. Xiao, U. Lienert, Forward modeling method for microstructure reconstruction using x-ray diffraction microscopy: single-crystal verification, Rev. Sci. Instrum. 77 (12) (2006) 123905.
[40] S. Li, J. Lind, C. Hefferan, R. Pokharel, U. Lienert, A. Rollett, R. Suter, Three-dimensional plastic response in polycrystalline copper via near-field high-energy X-ray diffraction microscopy, J. Appl. Crystallogr. 45 (6) (2012) 1098–1108.
[41] S. Li, R. Suter, Adaptive reconstruction method for three-dimensional orientation imaging, J. Appl. Crystallogr. 46 (2) (2013) 512–524.
[42] A.D. Spear, S.F. Li, J.F. Lind, R.M. Suter, A.R. Ingraffea, Three-dimensional characterization of microstructurally small fatigue-crack evolution using quantitative fractography combined with post-mortem X-ray tomography and high-energy X-ray diffraction microscopy, Acta Mater. 76 (2014) 413–424.
[43] M.D. Uchic, M.A. Groeber, D.M. Dimiduk, J. Simmons, 3D microstructural characterization of nickel superalloys via serial-sectioning using a dual beam FIB-SEM, Scr. Mater. 55 (1) (2006) 23–28.
[44] M. Groeber, B. Haley, M. Uchic, D. Dimiduk, S. Ghosh, 3D reconstruction and characterization of polycrystalline microstructures using a FIB-SEM system, Mater. Charact. 57 (4) (2006) 259–273.
[45] G. Spanos, D. Rowenhorst, A. Lewis, A. Geltmacher, Combining serial sectioning, EBSD analysis, and image-based finite element modeling, MRS Bull. 33 (6) (2008) 597–602.
[46] H. Sharma, S.M. Van Bohemen, R.H. Petrov, J. Sietsma, Three-dimensional analysis of microstructures in titanium, Acta Mater. 58 (7) (2010) 2399–2407.
[47] M.P. Echlin, A. Mottura, C.J. Torbet, T.M. Pollock, A new TriBeam system for three-dimensional multimodal materials analysis, Rev. Sci. Instrum. 83 (2) (2012) 023701.
[48] A. King, P. Reischig, J. Adrien, W. Ludwig, First laboratory X-ray diffraction contrast tomography for grain mapping of polycrystals, J. Appl. Crystallogr. 46 (6) (2013) 1734–1740.